SCIENCE CHINA
Chemistry

•ARTICLES•

March 2019 Vol.62 No.3: 385–392
https://doi.org/10.1007/s11426-018-9395-1

Covalent organic frameworks derived hollow structured *N*-doped noble carbon for asymmetric-electrolyte Zn-air battery

Pingwei Cai[1,2], Xinxin Peng[1,2], Junheng Huang[1], Jingchun Jia[1], Xiang Hu[1] & Zhenhai Wen[1*]

[1]*CAS Key Laboratory of Design and Assembly of Functional Nanostructures, Fujian Provincial Key Laboratory of Nanomaterials, Fujian Institute of Research on the Structure of Matter, Chinese Academy of Sciences, Fuzhou 350002, China;*
[2]*University of Chinese Academy of Science, Beijing 100049, China*

Received November 6, 2018; accepted November 27, 2018; published online January 31, 2019

We report a relatively low-temperature molten salt strategy to prepare hollow structured *N*-doped noble carbon (h-NNC) with highly desirable features of ultra-large surface area (1957 $m^2 g^{-1}$) and high graphitization, endowing the h-NNC with high activity toward catalysis of oxygen reduction reaction in acidic medium. The h-NNC is applied as cathode catalyst of an asymmetrical-electrolyte Zn-air battery, which exhibits an open circuit voltage of 2.11 V, a power density up to 270 mW cm^{-2}, and an energy density of 1279 W h kg^{-1}, behaving advantages over the conventional Zn-air batteries.

noble carbon, oxygen reduction reaction, asymmetric-electrolyte Zn-air battery, energy density

Citation: Cai P, Peng X, Huang J, Jia J, Hu X, Wen Z. Covalent organic frameworks derived hollow structured *N*-doped noble carbon for asymmetric-electrolyte Zn-air battery. *Sci China Chem*, 2019, 62: 385–392, https://doi.org/10.1007/s11426-018-9395-1

1 Introduction

Zn-air batteries (ZABs) have attracted massive attention due to their high theoretic energy density, which are considered as a prospective technology to meet the energy requirements for future electric vehicles and utility-scale energy storage system [1–4]. However, the cell voltage and energy density in the ZABs reported so far were still far away from satisfactory for the practical application. Therefore, it is highly essential to further improve the output voltage and energy density of ZABs [5,6]. The optimization of each unit's design (i.e., electrode, membrane, electrolyte) plays a significant role in advancing the ZABs performance [7,8]. In our previous work [9], we proposed an asymmetric-electrolyte Zn-air battery (AEZAB) with commercial Pt/C as air-cathode catalyst in acidic medium that can be capable of improving the performance of ZABs with enhanced operation voltage, power density and energy density, exhibiting great prospects in filling up the ever-increasing demand of energy. However, the precious Pt and its alloys, due to their scarcity and high cost [10,11], are not the ideal candidates as the cathode electrocatalysts [12,13], thus calling for the development of precious metal free electrocatalysts that show high activity toward oxygen reduction reaction (ORR) in acidic solution to fulfil the practical application of such device [14–17].

In recent years, noble-metal free or even metal free ORR catalysts have been developed and showed impressive ORR activity in alkaline solution [18–25]. Among them, noble nanocarbons, as an emerging but promising material, hold great promise for the ORR thanks to large surface area and flexible dopants [26–30]. Unfortunately, they likely perform inferior in acidic electrolyte due to the insufficient active sites and poor stability [31,32]. In this regard, it still remains grand challenge in design and synthesis of nanocarbons with features of ultra-large surface area and high graphitization, these merits are of great importance for enhancing the number of catalytic activity sites and improving the operating stability. To achieve an ultrahigh surface area, it normally

*Corresponding author (email: Wen@fjirsm.ac.cn)

requires the assistance of templates or strong base for nanocarbon synthesis [33–36]; while preparation of high-quality graphite carbon typically need a high carbonization temperature up to 2000 °C [37]; even though the temperature can be lowered to below 1000 °C with assistance of catalysts (e.g., Fe, Co, Ni), the removing of the residue catalysts nanoparticles is a very tricky issue [38].

Herein, we report a template-free molten salt strategy to synthesize hollow structured nitrogen-doped noble carbon (h-NNC) that feature ultrahigh surface area of up to 1957 $m^2 g^{-1}$ and high-quality graphite structure, the synthesis is notably implemented without the assistance of catalyst at a rather low temperature. Moreover, the as-developed noble carbon catalysts, thanks to the large surface area, uniform pore distribution and high graphitization, exhibit catalytic activities approaching to the Pt/C catalyst towards ORR in acidic medium. We further verify the h-NNC is a promising low-cost cathode material for asymmetric-electrolyte Zn-air battery (AEZAB), which is capable of affording an open circuit voltage of 2.11 V, a power density of 270 mW cm^{-2}, and an energy density of 1279 W h kg^{-1}.

2 Results and discussion

For the preparation of the h-NNC, the covalent organic frameworks (COFs) precursor were synthesized by polymerization of 1,4-dicyanobenzene monomer with the assistance of molten $ZnCl_2$ in vacuum followed by carbonization treatment in Ar atmosphere (Scheme 1).

The samples are denoted as h-NNC-*X* (*X* is the carbonization temperature). The scanning electron microscope (SEM) images of the h-NNC-1150 demonstrate that there are a great deal of distinct pores with size of below 50 nm on the surface of the sample (Figure 1(a, b)), which can be further evidenced by the magnified SEM images (Figure S1, Supporting Information online). The transmission electron microscope (TEM) tests were carried out to illustrate the porous structure. Figure 1(c) exhibits a typical TEM image of the h-NNC-1150, revealing the samples consist of lots of nanopores with cavity size varying from 5 to 20 nm, as verified by more TEM images (Figures 1(d) and S2). Figure 1(e, f) presents the high-resolution TEM images of the h-NNC-1150, reconfirming the nano-pore structure is actually composed of highly-crystalline graphite outer ring, as demonstrated by the interplanar crystalline space of 0.34 nm and distinct lattice fringe (Figure 1(h)). The samples prepared at other temperatures, i.e., 950, 1050 and 1250 °C, show similar morphology to that of h-NNC-1150 (Figure S3).

To investigate the formation mechanism of the unique noble carbon nano-frame, we prepared a set of control samples by carbonizing precursor COFs at 1150 °C without the assistance of molten $ZnCl_2$ (NC-1150). Based on the

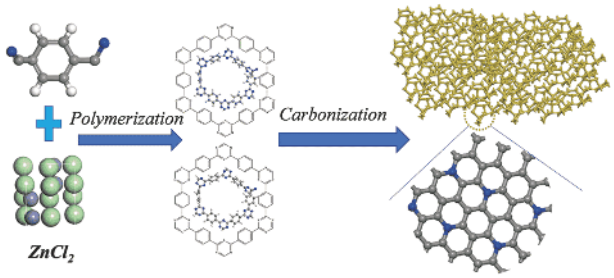

Scheme 1 Schematic graph of preparation of h-NNC (color online).

thermogravimetric analysis (TGA, Figure S4), we could conclude that the h-NNC-1150 can even maintain stable in air atmosphere up to 600 °C, while the COFs precursor and NC-1150 were easily oxidized at a rather low temperature, indicating the more nobility of h-NNC-1150 [39,40]. With the assistance of $ZnCl_2$, the precursor can generate well-defined hollows structure and indistinct lattice fringe (Figure S5) at a low temperature of 650 °C. Whereas, agglomerated nanoparticles, rather than porous frameworks structure, were formed in the NC-1150 samples (Figure S6(a, b)). Moreover, one cannot well observe lattice fringes in the high-resolution transmission electron microscope (HRTEM) images of NC-1150 (Figure S6(c)), which is consistent with the result of selected area electron diffraction (SAED) pattern (Figure S6 (d)). These results strongly evidenced that the molten $ZnCl_2$ not only serves as porogen and solvent to enhance the evolution of porous hollow structure, but also is beneficial to promote the formation of high-quality graphite [41,42], thanks to the advantages of better local dynamics, heat exchange for the molten salt method [43,44]. Moreover, the further carbonization of the COFs can contribute to the generation of the noble, nitrogen-doped carbon and result in highly sp^2 hybridization of carbon atom [39].

N_2 adsorption-desorption measurements were further carried out to evaluate the specific surface area and pore size distribution of the h-NNCs. The BET surface area is 1644 $m^2 g^{-1}$ for h-NNC-950, 1885 $m^2 g^{-1}$ for h-NNC-1050, 1957 $m^2 g^{-1}$ for h-NNC-1150, and 1546 $m^2 g^{-1}$ for h-NNC-1250, respectively (Table S1, Supporting Information online). Figure 2(a) presents the N_2 adsorption-desorption curves of the h-NNC-1150, and the sample shows a typical IV pattern with a rapid nitrogen uptake at P/P_0<0.1, implying the existence of microporous structure, which is further proved by the peak located at 0–2 nm in the pore size distribution curves derived from the N_2 desorption branches (Figure 2(b)). Furthermore, the obvious hysteresis loop was observed due to the presence of mesopores, being consistent with the results of HRTEM and pore-size distribution curve. In addition, one can observe the pore size distribution ranges from 0–8 nm for the h-NNC-950, h-NNC-1050 and h-NNC-1250 (Figure 2(b)), suggesting the optimized temperature of 1150 °C would generate a favourable porous structure and a

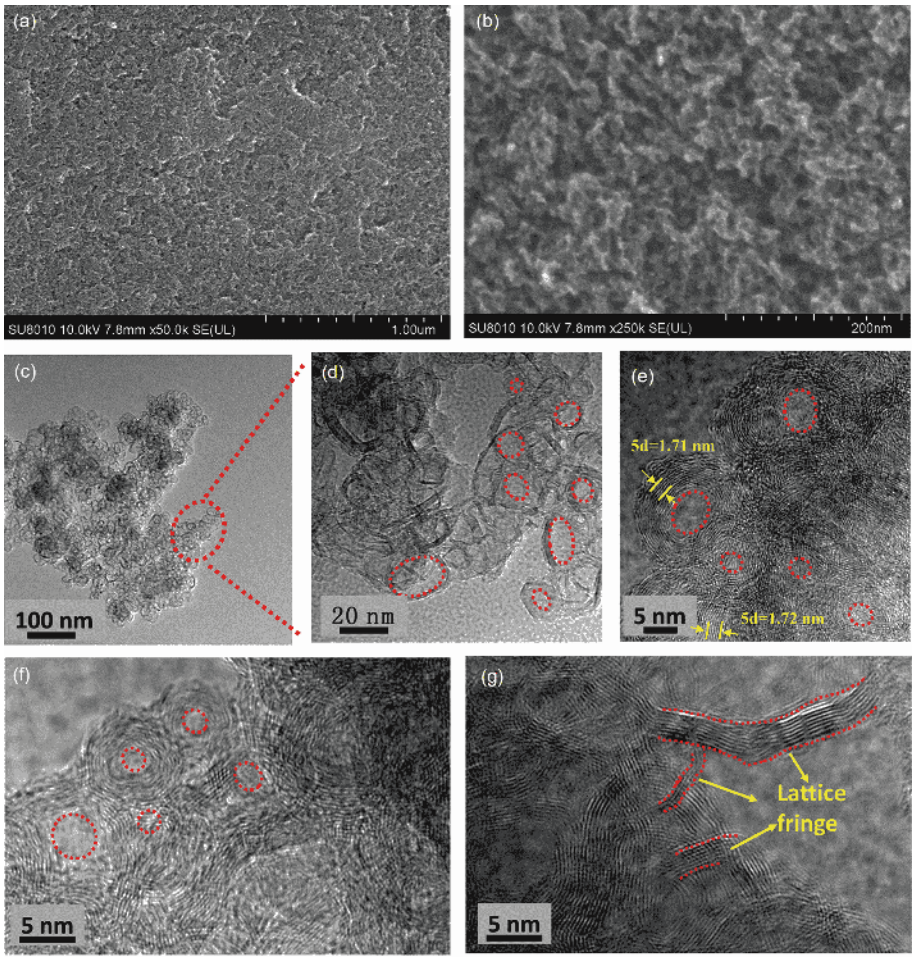

Figure 1 (a, b) SEM images, (c, d) TEM images and (g, f, h) HRTEM images of h-NNC-1150 (color online).

considerably high BET surface area.

We also conducted Raman spectra to further investigate the intrinsic structure properties. Figure 2(c) shows the Raman spectra for the set of h-NNC samples, in which one can see two peaks at ~1375 and ~1595 cm^{-1}, being indicative of defective carbon (sp^3) and graphite carbon (sp^2) atoms. The value of density ratio of defective and graphite carbon atoms (I_D/I_G) is usually employed to evaluate the defect density in carbon materials [45]. The h-NNC-1150 possesses the modest value of I_D/I_G compared to other h-NNC, suggesting that h-NNC-1150 may exhibit more desirable electrochemical activity for ORR since that h-NNC-1150 has optimal conductivity and defects. The composition information of the products was studied by the X-ray photoelectron spectroscopy (XPS). All the h-NNCs samples contain C, N, O elements based on the survey XPS spectra (Figure S7), and the element content was shown in Table S2. The N content decreased with the increase of temperature. Figure 2(d) displays the high-resolution XPS spectra of N 1s of the set of h-NNC samples. The peaks located at 398.3, 399.5, 401.2 and 40.2.1 eV were assigned to pyridinic N, pyrrolic N, graphitic N and oxidized N, respectively [46–49]. The curves fitted in Figure 2(d) and Figure S8 suggest that a conversion from oxidized, pyridinic and pyrrolic to graphitic nitrogen with increasing temperature and the graphitic nitrogen become the dominant composition [50].

We first evaluated the catalytic activity of the set of catalysts toward ORR in acidic electrolyte. The cyclic voltammetry (CV) curves exhibit featureless peak within the whole potential window in an Ar-saturated 0.5 M H_2SO_4, while the well-defined peaks of 0.68 and 0.7 V for h-NNC-1150 and Pt/C emerged in O_2-saturated 0.5 M H_2SO_4 (Figure S9(a)), suggesting a significant ORR activity of the product. The ORR performances of as-synthesized catalysts were further investigated by linear sweep voltammetry (LSV) technique performed on rotating disk electrode (RDE) at a scan rate of 5 mV s^{-1}. As shown in Figure 3(a), the h-NNC-1150 obviously shows a more positive onset potential (E_0) and a lager limiting current density (j_L) than the other h-NNC samples. Specifically, an E_0 of 0.84 V and a half-wave potential ($E_{1/2}$) of 0.67 V have been achieved for the h-NNC-1150 with a j_L of 5.15 mA cm^{-2}. These performance parameters are comparable to the performance of the Pt/C catalyst (E_0 of 0.85 V, $E_{1/2}$ of 0.75 V and j_L of 5.21 mA cm^{-2}),

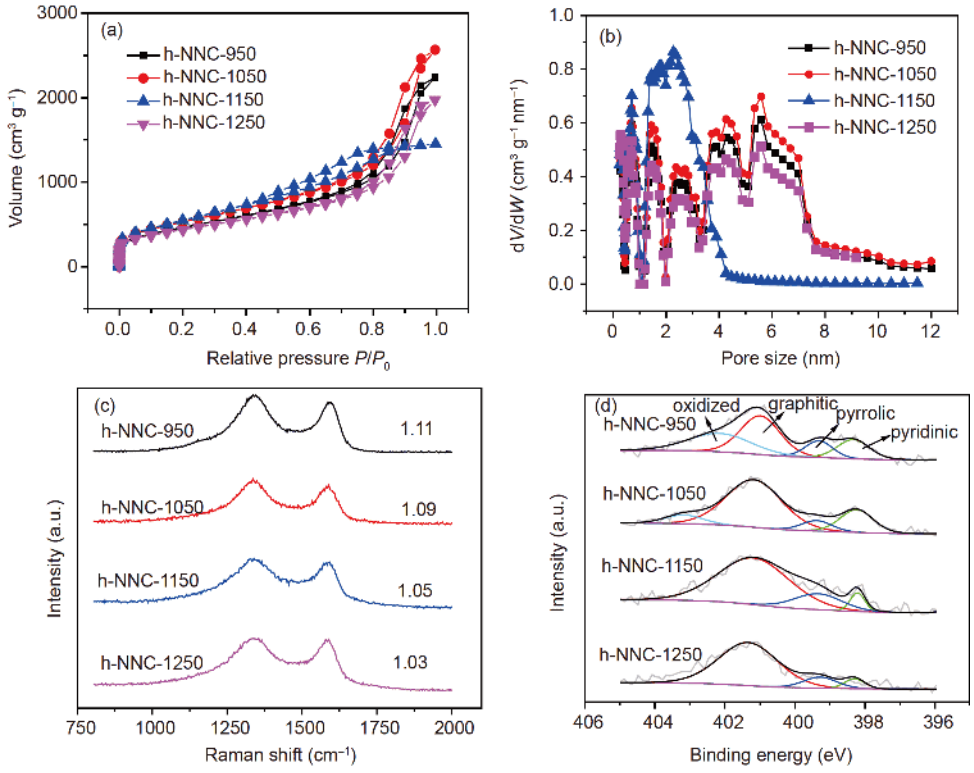

Figure 2 (a) N_2 adsorption curves, (b) pore size distribution curve, (c) Raman spectroscopy, and (d) high-resolution XPS spectra of N 1s of h-NNCs (color online).

indicating the excellent electrocatalytic activity towards ORR in the h-NNC-1150 (Figure 3(b)), which may be attributed to the enhanced electrochemical active area (Figure S9(b–f)). Whereas, the NC-1150 and the COF precursor performed inferior to those of h-NNC-1150 in terms of E_0, $E_{1/2}$ as well as j_k for ORR (Figure S10), confirming that the molten $ZnCl_2$ assistance in the synthesis could enhance the conductivity and active sites (Figure S11) of the products.

To obtain an insight to the reaction kinetics for ORR, Tafel curves were provided in Figure 3(c). The h-NNC-1150 shows a low Tafel slope of 70 mV dec^{-1}, much lower than that of other h-NNCs and Pt/C catalysts, demonstrating that the h-NNC-1150 undergoes a fast kinetics process towards ORR. Whereafter, rotating disk electrode (RDE) measurements were carried out to further determine the kinetics of the h-NNC-1150. Figure 3(d) shows the LSV curves of the h-NNC-1150 at different rotating speeds, in which the current density increases along with increasing the rotating speed. Moreover, the K-L plots also show good linearity and parallelism at different potentials (inset of Figure 3(d)), suggesting first-order reaction kinetics towards ORR in regard to the concentration of dissolved O_2.

To further estimate the ORR pathways for the h-NNCs, we conducted rotating ring-disk electron (RRDE) measurements (Figure S12). All the h-NNCs display a considerably low ring current that arisen from H_2O_2 oxidation, in the manner of 4-electron transferring with producing water. Figure 3(e) illustrates the transfer electron number (n) and H_2O_2 production of h-NNCs for ORR based on RRDE measurements. A nearly 4 electron transfer number (over 3.9) and a small ratio of H_2O_2 production (less than 7%) further demonstrate that the h-NNC-1150 favours a four-electron pathway to produce water upon ORR catalysis. The stability of the catalysts was investigated by chronoamperometric technique in the O_2-staturated 0.5 M H_2SO_4 at the fixed potential of 0.6 V. The h-NNC-1150 exhibits a slight current decrease of about 7% after 20000 s, less than that of Pt/C (11%, Figure 3(f), top), suggesting a decent stability in acids. Compared to the Pt/C catalyst, the h-NNC-1150 also shows good tolerance to methanol with slight oscillation in the ORR process upon adding methanol (Figure 3(f), bottom).

In addition, we further assessed the ORR performance of h-NNCs in neutral and alkaline solutions. Interestingly, the h-NNC-1150 also exhibits excellent performance, affording an E_0 of 0.91 V and an $E_{1/2}$ of 0.77 V with a large j_L of ~6.0 mA cm^{-2}, displaying a low Tafel slope of 142 mV dec^{-1}, showing a four-electron transfer process for ORR and low H_2O_2 yield in 0.1 M PBS (pH 7.0), which are superior to those of other h-NNCs, and even beat commercial Pt/C (Figures 4(a, b) and S13). When carried out in 0.1 M O_2-saturated KOH solution, the h-NNC-1150 shows a more positive E_0 of 0.99 V and $E_{1/2}$ of 0.87 V, larger j_L of 5.8 mA cm^{-2} and lower Tafel slope of 66 mV dec^{-1} compared to other h-NNCs and Pt/C. The electron transfer

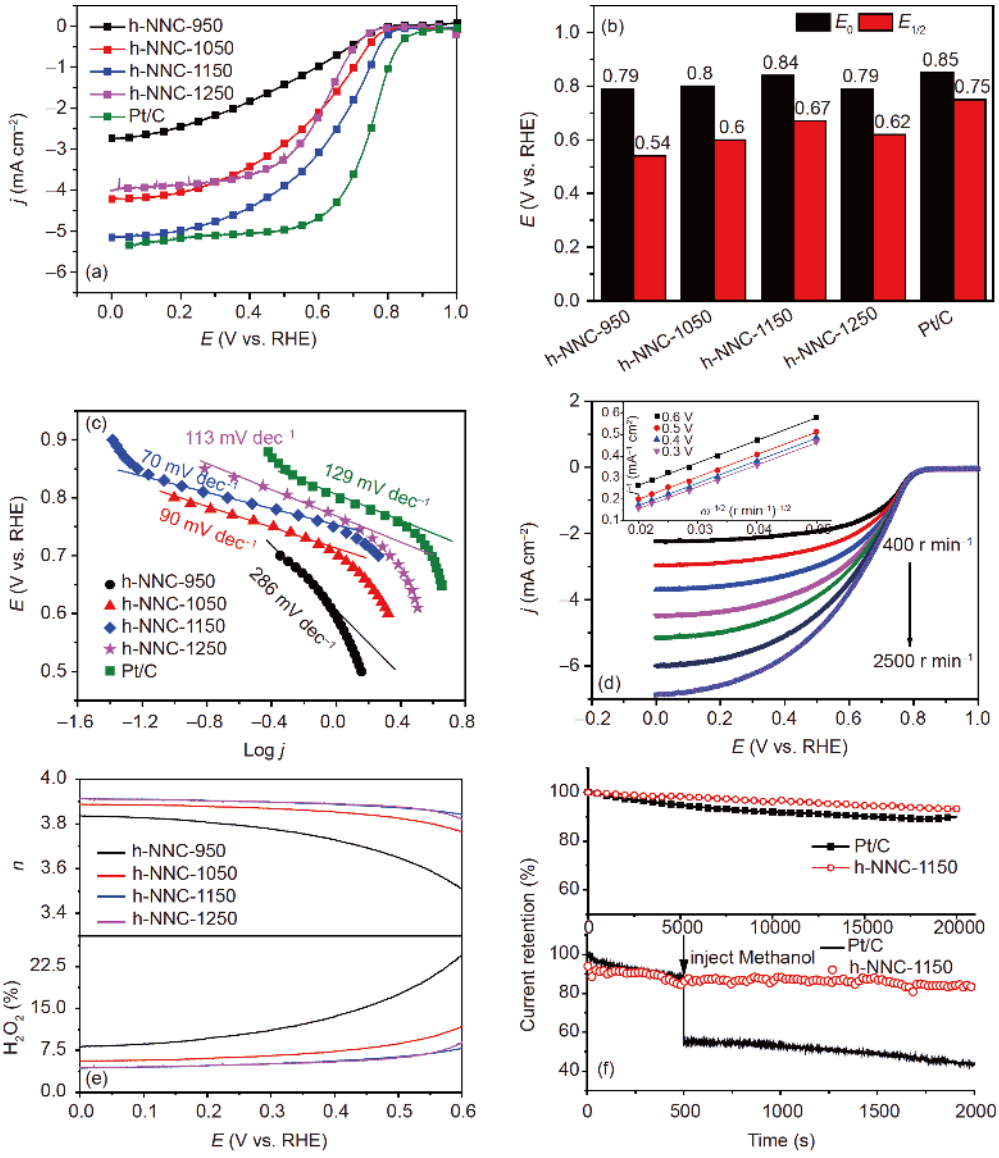

Figure 3 (a) LSV curves at a scan rate of 5 mV s^{-1} under a rotating rate of 1600 r min^{-1}; (b) graph of onset potential and half-wave potential; (c) Tafel plots of various h-NNCs and Pt/C catalysts in O_2-saturated 0.5 M H_2SO_4 solution; (d) LSV curves of h-NNC-1150 at different rotating speeds (the inset is K-L plots of h-NNC-1150 at different potentials); (e) transfer electron number and H_2O_2 production of h-NNC and Pt/C catalysts, respectively, which were calculated from RRDE measurements; (f) current retention-time (top) and chronoamperometric responses of Pt/C and h-NNC-1150 before and after adding 5 mL methanol into 50 mL 0.5 M H_2SO_4 (bottom) (color online).

number and H_2O_2 yield were calculated to be greater than 3.8 and less than 10% in the applied potential windows based on RRDE measurements (Figures 4(c, d) and S14), applying that it undergoes a four-electron transfer reduction process with high selectivity. The outstanding catalytic activity of h-NNCs in all-pH media not only beat many metal-free catalysts, but also be comparable to that of metal-based materials. The detailed comparisons are presented in Tables S3–S5, further demonstrating the prominent electrocatalytic activity towards ORR.

We built an asymmetrical-electrolyte Zn-air battery (AEZAB) with zinc plate as anode plugging in 4.0 M NaOH anolyte and the h-NNC-1150 based electrode as cathode dipping in 2.0 M H_2SO_4 catholyte, which were separated by a bipolar membrane (BPM) (Figure 5(a)). With such design, the AEZAB can deliver an open circuit voltage of 2.55 V with a specific energy density of 2091 W h kg^{-1} in theory, thanks to the electrochemical neutralization energy originating from the pH gradient between anolyte and catholyte, showing remarkable advantages over the traditional ZAB that only possesses an open circuit voltage of 1.65 V and a theoretical energy density of 1361.2 W h kg^{-1}.

We first evaluated the performance of the AEZAB by examining the open circuit voltage (V_{OC}) with the h-NNC-1150 as cathode. For comparison, a conventional single chamber ZAB was built up with 4.0 M NaOH as electrolyte

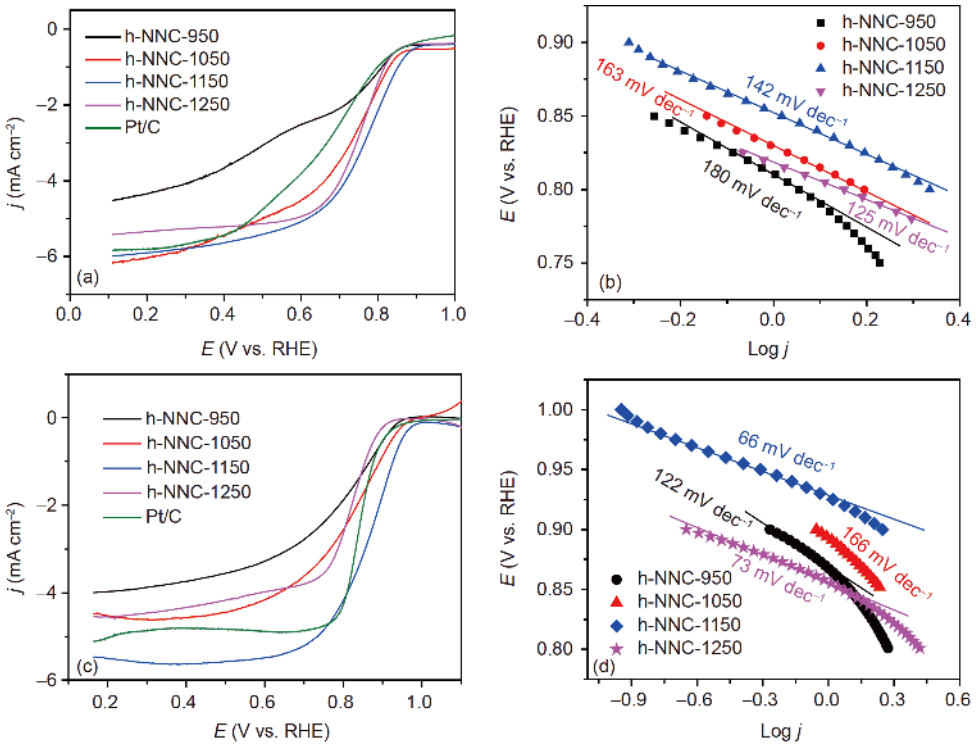

Figure 4 (a, c) LSV curves and (b, d) Tafel plots of various ORR catalysts. (a, b) in 0.1 M PBS; (c, d) in 0.1 M KOH (color online).

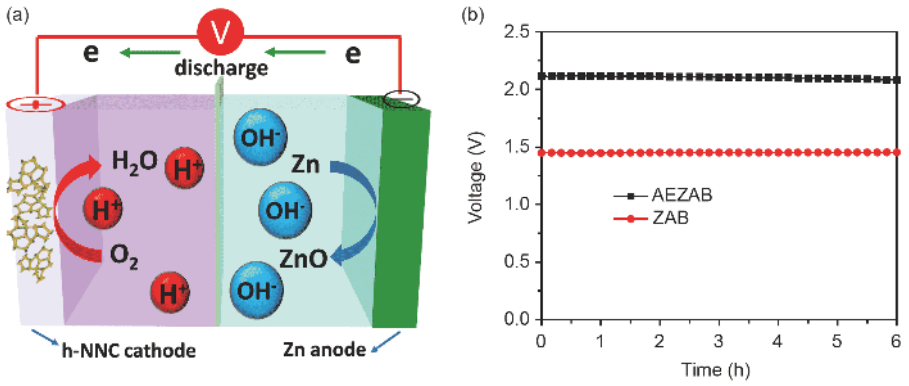

Figure 5 (a) Schematic graph of as-built asymmetry-electrolyte Zn-air battery (AEZAB); (b) open circuit voltage for AEZAB and conventional ZAB with h-NNC-1150 as cathode catalyst (color online).

of the anode and the cathode chamber. The V_{OC} of the h-NNC-1150-based AEZAB can reach 2.11 V, 0.67 V higher than that of the conventional ZAB (1.45 V) (Figure 5(b)), implying that the rational design of construction can effectively improve the V_{OC} of ZAB. Moreover, the voltages of the AEZAB are higher than that of ZAB at the same discharge current density (Figure S15), further demonstrating the asymmetrical design can enhance the cell voltage.

The maximum power density is considered as one of the most important parameters to examine whether the Zn-air battery can afford the peak load. Figure 6(a) displays the polarization curves and power density plots for the h-NNC-1150-based AEZAB and the conventional ZAB, respectively. The AEZAB can deliver a high maximum power density of 270 mW cm^{-2}, 1.88 times higher than that of conventional ZAB (143 mW cm^{-2}) and even beats the most outstanding ZABs reported before [51–54], further validating the proof that the asymmetric-electrolyte design in ZAB can bring about prominent promotion in performance. We also built up a series of AEZAB using various h-NNCs as cathode catalysts with the same construction. As shown in Figure S16, the h-NNC-1150-AEZAB still exhibits the most favourable performance compared the other AEZABs, further indicating the preeminent electrocatalytic activity towards ORR for h-NNC-1150 in acid medium.

We further assessed the specific capacity and the energy

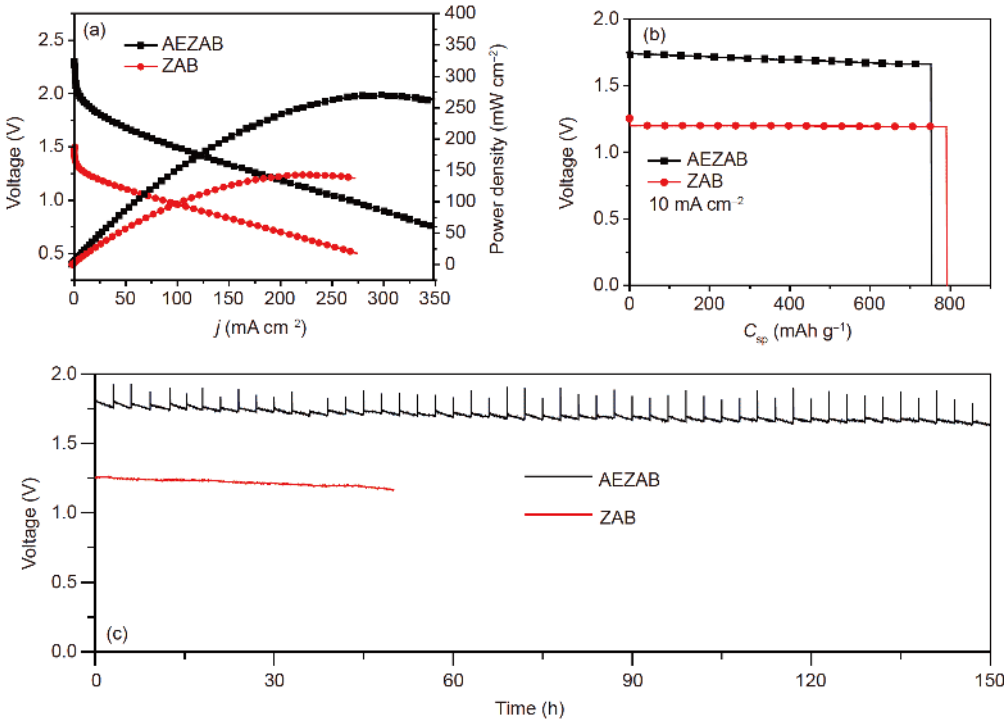

Figure 6 (a) Discharge polarization and power density curves; (b) voltage vs. specific capacities plots; (c) long term stability test for AEZAB and conventional ZAB with h-NNC-1150 as cathode catalyst, respectively (color online).

density for AEZAB and conventional ZAB, respectively. As the discharge curves of AEZAB and conventional ZAB at 10 mA cm^{-2} shown in Figure S17, the h-NNC-1150-based AEZAB exhibits a higher voltage (~1.75 V) than that of conventional ZAB (less than 1.25 V). The specific capacity of the h-NNC-1150-based AEZAB is estimated to be 754 mA h g^{-1}. This value is slightly less than that of the conventional ZAB (792 mA h g^{-1}, Figure 6(b)), which is due to the inferior ORR activity in acidic environment compared to that in alkaline solution. The energy density is calculated to be 1279 W h kg^{-1} for h-NNC-1150-based AEZAB by integration of the voltages vs. specific capacities curve, 1.35 times higher than that of conventional ZAB (947 W h kg^{-1}), and also be comparable to theoretic energy density of ZAB (1361 W h kg^{-1}). In a word, the AEZAB shows predominant advantages in terms of working voltage, power density and energy density, manifesting a huge potential for the high-energy and high-voltage applications.

The long-term durability test was conducted by galvanostatic discharge at a current density of 10 mA cm^{-2} for continuously running for 150 h with refreshing the electrolytes every 3 h (Figure 6(c)). The AEZAB can maintain a relatively stable voltage of 1.6–1.8 V to deliver a constant current density of 10 mA cm^{-2} provided refreshing the electrolytes. Since the electrochemical neutralization energy is generated by consuming H^+ in cathode and OH^- in anode respectively, the voltage will deduce after long-term operation because of the continue consumption of H^+ and OH^-, so we need to continuously refresh the electrolyte. Nevertheless, the as-proposed idea holds attractive advantages over the conventional Zn-air battery with enhance operating voltage and power density, although we confess that they are still in an infant stage.

To investigate influence of the electrolyte on the battery performance, we constructed several AEZABs with various catholytes. When the cathode chamber was filled with 4.0 M NaOH or 1.0 M PBS solution, the corresponding AEZAB behaves a prominent decline in V_{OC} and power density (Figure S18), suggesting that cell performance is related to the pH differentials between anolyte and catholyte, which can significantly affect the electrochemical neutralization energy. It is noted that the asymmetric-electrolyte Zn-air battery can achieve more excellent performance using Pt/C as cathode catalyst, exhibiting a V_{OC} of 2.25 V, a peak power density of 380 mW cm^{-2}, and an energy density of 1522 W h kg^{-1} (Figure S19)

3 Conclusions

In summary, we have developed a straightforward molten salt assisted method for preparation of hollow structured *N*-doped noble carbon (h-NNC) by carbonization of covalent organic frameworks. The as-result h-NNC possesses a large specific surface area of 1957 m^3 g^{-1} and a high graphite crystalline structure; these unique features endow it with

highly desirable as electrocatalysts for ORR. An asymmetric electrolytes Zn-air battery was built with h-NNC as cathode catalysts, exhibiting an open circuit voltage of 2.11 V, a maximum power density of 270 mW cm^{-2} and an energy density of 1279 W h kg^{-1}. The results indicate that the catalyst design and device construction in Zn-air battery will have great impacts on the performance of Zn-air battery. The strategy not only opens a venue to improve the performance of Zn-air battery, but also provides more feasibility considerations for the design of novel energy storage and conversion devices.

Acknowledgements This work was supported by the 1000 Plan Professorship for Young Talents, Hundred Talents Program of Fujian Province, the Fujian Science and Technology Key Project (2016H0043), and the National Natural Science Foundation of China (21703249, 21701175).

Conflict of interest The authors declare that they have no conflict of interest.

Supporting information The supporting information is available online at http://chem.scichina.com and http://link.springer.com/journal/11426. The supporting materials are published as submitted, without typesetting or editing. The responsibility for scientific accuracy and content remains entirely with the authors.

1 Li Y, Dai H. *Chem Soc Rev*, 2014, 43: 5257–5275
2 Lee JS, Tai Kim S, Cao R, Choi NS, Liu M, Lee KT, Cho J. *Adv Energy Mater*, 2011, 1: 34–50
3 Zhang J, Zhao Z, Xia Z, Dai L. *Nat Nanotech*, 2015, 10: 444–452
4 Lee DU, Choi JY, Feng K, Park HW, Chen Z. *Adv Energy Mater*, 2014, 4: 1301389
5 Cao R, Lee JS, Liu M, Cho J. *Adv Energy Mater*, 2012, 2: 816–829
6 Cheng F, Chen J. *Chem Soc Rev*, 2012, 41: 2172–2192
7 Wang ZL, Xu D, Xu JJ, Zhang XB. *Chem Soc Rev*, 2014, 43: 7746–7786
8 Li L, Liu C, He G, Fan D, Manthiram A. *Energy Environ Sci*, 2015, 8: 3274–3282
9 Cai P, Li Y, Chen J, Jia J, Wang G, Wen Z. *ChemElectroChem*, 2018, 5: 589–592
10 Lukowski MA, Daniel AS, Meng F, Forticaux A, Li L, Jin S. *J Am Chem Soc*, 2013, 135: 10274–10277
11 Yin Y, Han J, Zhang Y, Zhang X, Xu P, Yuan Q, Samad L, Wang X, Wang Y, Zhang Z, Zhang P, Cao X, Song B, Jin S. *J Am Chem Soc*, 2016, 138: 7965–7972
12 Wang YJ, Zhao N, Fang B, Li H, Bi XT, Wang H. *Chem Rev*, 2015, 115: 3433–3467
13 Zhang H, Hwang S, Wang M, Feng Z, Karakalos S, Luo L, Qiao Z, Xie X, Wang C, Su D, Shao Y, Wu G. *J Am Chem Soc*, 2017, 139: 14143–14149
14 Ma J, Xiang Z, Zhang J. *Sci China Chem*, 2018, 61: 592–597
15 Liu X, Park M, Kim MG, Gupta S, Wang X, Wu G, Cho J. *Nano Energy*, 2016, 20: 315–325
16 Sun M, Zhang G, Liu H, Liu Y, Li J. *Sci China Mater*, 2015, 58: 683–692
17 Cai P, Hong Y, Ci S, Wen Z. *Nanoscale*, 2016, 8: 20048–20055
18 Yan D, Guo L, Xie C, Wang Y, Li Y, Li H, Wang S. *Sci China Mater*, 2018, 61: 679–685
19 Cheng F, Zhang T, Zhang Y, Du J, Han X, Chen J. *Angew Chem Int Ed*, 2013, 52: 2474–2477
20 Yi QF, Zhang YH, Liu XP, Yang YH. *Sci China Chem*, 2014, 57: 739–747
21 Wen Z, Ci S, Zhang F, Feng X, Cui S, Mao S, Luo S, He Z, Chen J. *Adv Mater*, 2012, 24: 1399–1404
22 Zhang G, Jin X, Li H, Wang L, Hu C, Sun X. *Sci China Mater*, 2016, 59: 337–347
23 Zhou YX, Yao HB, Wang Y, Liu HL, Gao MR, Shen PK, Yu SH. *Chem Eur J*, 2010, 16: 12000–12007
24 Miura A, Rosero-Navarro C, Masubuchi Y, Higuchi M, Kikkawa S, Tadanaga K. *Angew Chem Int Ed*, 2016, 55: 7963–7967
25 Liang HW, Wei W, Wu ZS, Feng X, Müllen K. *J Am Chem Soc*, 2013, 135: 16002–16005
26 Wu G, More KL, Johnston CM, Zelenay P. *Science*, 2011, 332: 443–447
27 Gong K, Du F, Xia Z, Durstock M, Dai L. *Science*, 2009, 323: 760–764
28 Wei W, Liang H, Parvez K, Zhuang X, Feng X, Müllen K. *Angew Chem Int Ed*, 2014, 53: 1570–1574
29 Elumeeva K, Fechler N, Fellinger TP, Antonietti M. *Mater Horiz*, 2014, 1: 588–594
30 Liang HW, Zhuang X, Brüller S, Feng X, Müllen K. *Nat Commun*, 2014, 5: 4973
31 Wu G, Zelenay P. *Acc Chem Res*, 2013, 46: 1878–1889
32 Malko D, Kucernak A, Lopes T. *J Am Chem Soc*, 2016, 138: 16056–16068
33 Ryoo R, Joo SH, Kruk M, Jaroniec M. *Adv Mater*, 2001, 13: 677–681
34 Liang C, Li Z, Dai S. *Angew Chem Int Ed*, 2008, 47: 3696–3717
35 Zhu Y, Li L, Zhang C, Casillas G, Sun Z, Yan Z, Ruan G, Peng Z, Raji ARO, Kittrell C, Hauge RH, Tour JM. *Nat Commun*, 2012, 3: 1225
36 Lv R, Cui T, Jun MS, Zhang Q, Cao A, Su DS, Zhang Z, Yoon SH, Miyawaki J, Mochida I, Kang F. *Adv Funct Mater*, 2011, 21: 999–1006
37 Huang W, Wang Y, Luo G, Wei F. *Carbon*, 2003, 41: 2585–2590
38 Wen Z, Ci S, Hou Y, Chen J. *Angew Chem Int Ed*, 2014, 53: 6496–6500
39 Antonietti M, Oschatz M. *Adv Mater*, 2018, 30: 1706836
40 Men Y, Siebenbürger M, Qiu X, Antonietti M, Yuan J. *J Mater Chem A*, 2013, 1: 11887–11893
41 Kuhn P, Thomas A, Antonietti M. *Macromolecules*, 2008, 42: 319–326
42 Kuhn P, Forget A, Su D, Thomas A, Antonietti M. *J Am Chem Soc*, 2008, 130: 13333–13337
43 Liu X, Fechler N, Antonietti M. *Chem Soc Rev*, 2013, 42: 8237–8265
44 Lin L, Ou H, Zhang Y, Wang X. *ACS Catal*, 2016, 6: 3921–3931
45 Ding Y, Tang Y, Yang L, Zeng Y, Yuan J, Liu T, Zhang S, Liu C, Luo S. *J Mater Chem A*, 2016, 4: 14307–14315
46 Ahn SH, Yu X, Manthiram A. *Adv Mater*, 2017, 29: 1606534
47 Zhang J, Qu L, Shi G, Liu J, Chen J, Dai L. *Angew Chem Int Ed*, 2015, 55: 2230–2234
48 Yang W, Liu X, Yue X, Jia J, Guo S. *J Am Chem Soc*, 2015, 137: 1436–1439
49 Song H, Yang L, Tang Y, Yan D, Liu C, Luo S. *Chem Eur J*, 2015, 21: 16631–16638
50 Liu Q, Wang Y, Dai L, Yao J. *Adv Mater*, 2016, 28: 3000–3006
51 Zhang J, Zhou H, Zhu J, Hu P, Hang C, Yang J, Peng T, Mu S, Huang Y. *ACS Appl Mater Interfaces*, 2017, 9: 24545–24554
52 Park J, Park M, Nam G, Lee J, Cho J. *Adv Mater*, 2015, 27: 1396–1401
53 Cai P, Ci S, Zhang E, Shao P, Cao C, Wen Z. *Electrochim Acta*, 2016, 220: 354–362
54 Wu X, Han X, Ma X, Zhang W, Deng Y, Zhong C, Hu W. *ACS Appl Mater Interfaces*, 2017, 9: 12574–12583